

On the impact of the temporal variability of the collisional quenching process on the mesospheric OH emission layer: A study based on SD-WACCM4 and SABER

S. Kowalewski¹, C. von Savigny², M. Palm¹, I.C. McDade³, and J. Notholt¹

¹Institute of Environmental Physics, University of Bremen, Bremen, Germany

²Institute of Physics, Ernst-Moritz-Arndt-University of Greifswald, Greifswald, Germany

³Department of Earth and Space Science & Engineering, York University, Toronto, Canada

Correspondence to: Stefan Kowalewski
kowalewski@iup.physik.uni-bremen.de

Abstract.

The mesospheric OH Meinel emissions are subject of many theoretical and observational studies devoted to this part of the atmosphere. Depending on the initial vibrational level of excitation the altitude of the considered OH Meinel emission is systematically shifted, which has important implications for the intercomparison of different studies considering different transition bands. Previous model studies suggest that these vertical shifts are essentially caused by the process of collisional quenching with atomic oxygen. Following this hypothesis, a recent study found experimental evidence of a coherent seasonality at tropical latitudes between vertical shifts of different OH Meinel bands and changes in atomic oxygen concentrations. Despite the consistent finding to the above mentioned hypothesis, it cannot be excluded that the actual temporal variability of the vertical shifts between different OH Meinel bands may in addition be controlled or even dominated by other processes. It remains an open question whether the observed temporal evolution is indeed mainly controlled by the modulation of the collisional quenching process with atomic oxygen. By means of a sensitivity study which employs a quenching model to simulations made with the SD-WACCM4 chemistry climate model, we aim at assessing this question. From this study we find that the observed seasonality of vertical OH Meinel shifts is only partially controlled by temporal changes in atomic oxygen concentrations, while molecular oxygen has another noticeable impact on the vertical OH Meinel shifts. This in particular becomes evident for the diurnal variability of vertical OH Meinel shifts, which reveal only a poor correlation with the atomic oxygen species. In addition, changes in the H + O₃ source gases provide another mechanism that can potentially affect the diurnal variability in addition. By comparison with limb radiance observations from the SABER/TIMED

satellite this provides an explanation for the less evident diurnal response between changes in O concentrations and vertical OH Meinel shifts. On the other hand, at seasonal time scales the coherency between both quantities is again evident in SABER/TIMED but less pronounced compared to our
25 model simulations.

1 Introduction

The hydroxyl (OH) emission layer is a prominent feature of the mesopause region. Its main production process is commonly referred to as the Bates–Nicolet mechanism (McDade, 1991). This mechanism suggests the exothermic reaction between O_3 and H, which leads to rotationally-vibrationally
30 excited OH radicals (Bates and Nicolet, 1950). According to the available exothermic energy of this reaction, these radicals can have excited vibrational states up to the $\nu = 9$ quantum number. Lower vibrational states can be populated via spontaneous emission, but also through collisional quenching with ambient species. Hence, we can distinguish between different $OH(\nu)$ layers with respect to their vibrational excitation states.

35 Because different observational studies on the mesospheric OH Meinel emission rely on different transition bands, it is of general interest to understand systematic differences between the vertical profiles of the associated $OH(\nu)$ layers. As we know from previous rocket campaigns (e.g. see Baker and Stair Jr (1988) for a comprehensive compilation of rocket campaigns), systematic vertical shifts exist between these layers, while further studies have shown that collisional quenching with
40 ambient species is significantly affecting these shifts (e.g. Dodd et al., 1994; Makhlof et al., 1995, and Adler-Golden, 1997). In particular atomic oxygen is an effective quencher and its impact on the vertical distribution of different $OH(\nu)$ layers has been recently investigated by von Savigny et al. (2012). Based on a sensitivity study, which relies on an updated version of a quenching model by McDade (1991), they suggest that quenching with atomic oxygen causes an upward shift of
45 the individual $OH(\nu)$ layers with increasing vibrational state. In a follow-up study von Savigny and Lednyts'kyi (2013) provided experimental evidence that the vertical shifts between different OH bands are indeed correlated with the amount of atomic oxygen in the altitude range of the OH emission layer. Despite the consistent findings between both studies, it should be outlined that the simulated OH profiles by von Savigny et al. (2012) were limited to a single month based on the
50 MSIS climatology, while the effect of collisional O quenching has been considered by different scaling factors in the associated rate term. On the other hand, systematic changes in the vertical O_3 and H profiles will also affect the temporal variability of the vertical $OH(\nu)$ shifts and must be taken into account when discussing the impact of collisional quenching on the vertical structure of the $OH(\nu)$ layers. Thus, it remains an open question whether the temporal changes in the relative
55 vertical $OH(\nu)$ shifts are mainly driven by the temporal variability of the ambient quenching species, the source gases of OH or by a combination of both.

To investigate the importance of the temporal variability of the collisional quenching on the vertical $\text{OH}(\nu)$ shifts, this study established an updated quenching model that is applied to simulations made with the Whole Atmosphere Community Climate Model driven with Specified Dynamical fields (SD-WACCM4).
60

The emphasis of this study will be on the equatorial regions, where the large amplitude of the diurnal migrating tide has a strong impact on OH airglow and ambient temperatures (Shepherd et al., 2006). Many studies have reported evidence of a semi-annual oscillation in airglow observations that is associated with the large seasonal changes in the tidal amplitude. For instance, Marsh et al. (2006) show a pronounced semi-annual oscillation in SABER OH Volume-Emission-Rate (VER) measurements at equatorial latitudes. A similar seasonality was also recently shown for OH VER measurements from SCIAMACHY (SCanning Imaging SpectroMeter for Atmospheric CHartography) by von Savigny and Lednyts'kyi (2013). In addition, a semi-annual oscillation was also reported from HRDI observations (Yee et al., 1997) and ISIS-2 observations (Cogger et al., 1981) of the $\text{O}(^1\text{S})$ green line. Because the vertically integrated O concentration should be proportional to the integrated OH VER (see Eq.(2) in Mlynczak et al. (2013)), the same observed seasonal variability could also apply for the vertical $\text{OH}(\nu)$ shifts.
65
70

Based on the initial hypothesis that the collisional quenching with atomic oxygen is affecting the relative vertical $\text{OH}(\nu)$ shifts, we would therefore expect a coherent response in these shifts with the temporal evolution of the diurnal migrating tide. Accordingly, we focus on the seasonal and diurnal changes in the collisional quenching of OH with atomic oxygen. In addition, we will also consider the impact of collisional quenching with molecular oxygen, the second most efficient OH quencher after atomic oxygen (Adler-Golden, 1997). The advantage of our model approach is that we can deactivate the individual collisional quenching processes to study the associated impact on the relative vertical $\text{OH}(\nu)$ shifts. We compare these simulations with limb radiance observations from the SABER (Sounding of the Atmosphere by Broadband Emission Radiometry) instrument onboard of the TIMED (Thermosphere Ionosphere Mesosphere Energetics Dynamics) satellite and discuss the observed temporal variability of the vertical $\text{OH}(\nu)$ shifts with regard to our model results.
75
80

This paper is structured as follows. Section 2 introduces our OH quenching model and gives a brief summary on the SD-WACCM4 and SABER data. The methodology of our analysis on the relative vertical $\text{OH}(\nu)$ shifts is explained in Sect. 3. This is followed by a discussion on potential sources of error in Sect. 4. Based on a case example we reexamine important systematic features of the temporal variability of the OH emission layer and O quenching species in Sect.5 to establish an expectation on the temporal evolution of vertical $\text{OH}(\nu)$ shifts. In Sect. 6 we investigate the initial hypothesis on the role of collisional quenching on the vertical $\text{OH}(\nu)$ shifts by simulating the seasonal variability of the OH emission layer from the SD-WACCM4 data for different model assumptions. These simulations are then compared with experimental observations from SABER. Based on the same methods, the diurnal variability of the OH quenching process is investigated in
85
90

Sect. 7. We provide a summary of our results for the seasonal and diurnal variability of the relative vertical OH(ν) shifts in Sect. 8 and discuss their implications on the initial hypothesis.

2 Model and data description

2.1 Hydroxyl quenching model

A detailed description of the quenching model, which we use as a basis for our OH simulations, is given in McDade and Llewellyn (1988) and McDade (1991). Here, we limit our discussion to its primary key aspects and our adjustments to simulate absolute number densities of OH(ν).

As mentioned in the beginning, the Bates–Nicolet mechanism suggests the principal excitation mechanism of vibrationally excited OH according to the following reaction:



where k_1 denotes the rate constant of this reaction. The released exothermic energy of this reaction leads to a preferred vibrational excitation between $\nu = 6$ and $\nu = 9$. In accordance with von Savigny et al. (2012) we assume the following processes to populate lower vibrational states:

- radiative cascade from the initially populated higher levels



- collisional relaxation



with Q = O₂, N₂.

- complete OH removal



with Q = O, O₂, N₂.

Apart from these processes, the recombination of the perhydroxyl radical (HO₂) with atomic oxygen as being proposed by Krassovsky (1963) could provide another mechanism to form OH with vibrational excitations below $\nu \leq 6$ at the mesopause. Different opinions exist on the importance of this mechanism to the general OH formation (e.g. see Khomich et al., 2008, for a summary of different studies), though the recent study by Xu et al. (2012) implicates that its contribution is rather negligible for vibrational states above $\nu = 3$. As we will discuss later, the main emphasis of our study is on vibrational states above $\nu = 3$, accordingly we neglect this mechanism in our following considerations.

Following McDade (1991), Eq. (3) in von Savigny et al. (2012) describes the OH concentration for steady state conditions. Here, we adjust this expression as follows:

$$125 \quad [\text{OH}(\nu)] = \left(A(\nu) + \sum_{\text{Q}} k_L^{\text{Q}}(\nu)[\text{Q}] \right)^{-1} \times \left(P(\nu)\{k_1[\text{H}][\text{O}_3]\} + \sum_{\nu^*=\nu+1}^9 [\text{OH}(\nu^*)]\{A(\nu^*,\nu) + \sum_{\text{Q}} k_3^{\text{Q}}(\nu^*,\nu)[\text{Q}]\} \right) \quad (1)$$

where P is the nascent vibrational level distribution, $A(\nu)$ corresponds to the inverse radiative lifetime of OH and k_L^{Q} is the total rate constant for removal of OH in vibrational level ν through Reactions R3 and R4. Accordingly, we substitute the nascent production rate p in von Savigny et al. (2012) by the $P(\nu)\{k_1[\text{H}][\text{O}_3]\}$ rate term in the nominator of Eq. (1). In contrast to the work of von Savigny et al. (2012), we do not normalise Eq. (1) with respect to the $\nu = 9$ vibrational state, because we aim to calculate absolute number densities of $\text{OH}(\nu)$ to allow for a direct comparison with the observed VER by SABER. Therefore, we have to implement absolute rate constants as well as absolute inverse radiative lifetimes in Eq. (1).

For our present model simulations we use the constants listed in Table 1, assuming that multiquantum relaxation only applies for quenching with O_2 , while the less efficient N_2 quenching is limited to single-quantum relaxation only. If we apply these assumptions to Eq. (1), we get the following expression for OH as a function of vibrational state:

$$140 \quad [\text{OH}(\nu)] = \left(A(\nu) + k_L^{\text{O}_2}(\nu)[\text{O}_2] + k_L^{\text{N}_2}(\nu)[\text{N}_2] + k_L^{\text{O}}(\nu)[\text{O}] \right)^{-1} \times \left(P(\nu)\{k_1[\text{H}][\text{O}_3]\} + \sum_{\nu^*=\nu+1}^9 [\text{OH}(\nu^*)]\{A(\nu^*,\nu) + k_3^{\text{O}_2}(\nu^*,\nu)[\text{O}_2] + k_3^{\text{N}_2}(\nu^*,\nu)[\text{N}_2]\} \right) \quad (2)$$

with $k_3^{\text{N}_2}(\nu^*,\nu) = 0$ for all $\{\nu^* > \nu + 1\}$ and $k_3^{\text{N}_2}(\nu^*,\nu) = k_L^{\text{N}_2}(\nu^*)$ for $\{\nu^* = \nu + 1\}$.

2.2 SD-WACCM4

145 The SD-WACCM4 simulations are based on the Whole Atmosphere Community Model, version 4 (WACCM4), which is a comprehensive free running chemistry-climate model. This model version is based on an earlier version described by Garcia et al. (2007) and has been recently extended, such that it is nudged to meteorological fields that are taken from the Global Earth Observing System Model, Version 5 (GEOS-5) of NASA's Global Modeling and Assimilation Office (GMAO).

150 SD-WACCM4 data were provided to us by courtesy of R. R. Garcia and D. E. Kinnison, NCAR Boulder. The same SD-WACCM4 simulations, which we consider in our study, were already applied to another study by Hoffmann et al. (2012) that investigates the dynamics of the model using mesospheric CO VMR measurements. We therefore refer to this paper for a more detailed description of the model. Here, we limit our discussion to the most relevant aspects to our study.

155 The nudging of SD-WACCM4 with GEOS-5 meteorological fields is performed up to the 50 km
altitude level, followed by a linearly decreasing relaxation scheme until it completely switches to
a free-running mode above 60 km. Despite the limited altitude range of nudged meteorological
fields, Hoffmann et al. (2012) show that the upper (free-running) part is still strongly driven by the
described nudging and closely reflecting the dynamic response, which they deduce from CO based
160 measurements.

The horizontal resolution of the SD-WACCM4 data is $1.9^\circ \times 2.5^\circ$ in latitude and longitude. Its
vertical extent reaches from the ground up to the lower thermosphere at about 137 km geopotential
height (GPH) and it is divided into 66 height levels. The provided GPH values are transformed
to geometric heights for our analysis. In the region from 80 km up to 95 km, which encloses the
165 hydroxyl emission, the vertical distance between the model grid points varies from about 1.2 km to
3.6 km. The SD-WACCM4 simulations are initially performed at 0.5 h time increments, however,
to save computational resources, global model results are stored as daily increments at 00:00 UTC.
This limitation of our dataset prevents us from studying the diurnal evolution of the OH vertical
profiles at a fixed geolocation. To overcome this constraint we make the assumption that the diurnal
170 evolution of the vertical profiles is already contained within the zonal variation of each daily model
result, i.e. we convert the longitudinal information to the Local Solar Time (LST). However, as we
will discuss in Sect. 7.2, other processes exist, which can still complicate a direct comparison of the
diurnal variability between SD-WACCM4 and SABER.

To simulate $\text{OH}(\nu)$ profiles by means of Eq. (2), we convert the SD-WACCM4 chemical profiles
175 from VMR to absolute number densities based on the provided pressure and temperature fields. In
addition, we consider the SD-WACCM4 temperatures for the calculation of the temperature depen-
dent rate constant k_1 of reaction R1. The SD-WACCM4 data in this study cover the period between
April 2010 and June 2011.

2.3 SABER

180 SABER is a multichannel infrared radiometer onboard of the TIMED satellite. Limb profiles are
taken from a circular orbit at 625 km inclined at 74° to the equator and cover a latitudinal range
from 54° S to 82° N or 82° S to 54° N, depending on the phase of the yaw cycle (Russell III et al.,
1999). One yaw cycle of SABER corresponds to 60 days, i.e. due to the full precession of the
instrument during one cycle, this period is required to get a full coverage of local times.

185 SABER is equipped with two channels sensitive to OH emissions, i.e. the $1.6\mu\text{m}$ channel covers
emissions from the OH(5-3)/OH(4-2) transitions and the $2.0\mu\text{m}$ channel covers emissions from the
OH(9-7)/OH(8-6) transitions.

VER profiles from both channels are contained in the SABER Level 2a data products and will be
used in our study. According to Mertens et al. (2009) the vertical resolution of the SABER VER
190 profiles is approximately 2 km. Because the atmosphere is optically thin at altitudes above 80 km

for wavelengths between 0.35 and 2.0 μm (Khomich et al., 2008), the effect of self-absorption is negligible for the observed OH emission. Given this assumption, we can directly compare changes in our simulated OH concentrations to changes in the vertical VER profiles observed from both SABER channels.

195 In addition to measurements of the OH radiance, the latest SABER V2.0 data contain atomic oxygen profiles, which we use to study the impact of O quenching on the observed vertical shifts between the 1.6 μm and 2.0 μm VER profiles. As explained in Mlynczak et al. (2013), the SABER O concentrations are indirectly determined from the measured 2.0 μm VER profiles based on the steady state assumption:

$$200 \quad \underbrace{k_1[\text{H}][\text{O}_3]}_{\propto \text{VER}(2.0\mu\text{m})} = k_2[\text{O}][\text{O}_2] \quad (\text{R5})$$

with k_2 denoting the reaction rate constant between O and O₂ and $k_1[\text{H}][\text{O}_3]$ being directly proportional to the observed VER. At first glance, this seems to introduce a circular reasoning in our attempt to correlate O concentrations with the vertical shifts between the 1.6 μm and 2.0 μm VER profiles. This could potentially introduce a spurious (i.e. non-physical) correlation between both quantities, if the SABER model did not properly consider the real photochemistry and gaseous kinetics based on R5. However, Mlynczak et al. (2013) find a close agreement between their derived day- and nighttime O concentrations, which both rely on completely different methods. This indicates that the SABER model is reproducing physically meaningful O profiles. In turn, this should justify a direct comparison between SABER O concentrations and vertical shifts between both VER profiles, because we may suppose that any correlation between both quantities represents a real dependency between them.

3 Methodology

For the first part of this study we have to address some general features of the vertical OH profiles to provide a basis for our analysis on the collisional quenching process. Figure 1 shows vertical OH(ν) profiles that were simulated according to nighttime conditions at equatorial latitudes based on our model approach. In general, we will limit our discussion on the nighttime OH, because the relatively low abundances of daytime OH and the large Rayleigh scattering background makes a comparison with OH daytime observations more difficult.

220 In accordance with von Savigny et al. (2012) the vertical distribution of nighttime OH(ν) follows single peak profiles that are shifted upwards with respect to their vibrational state. If we normalise each OH(ν) profile, the relative vertical shifts become clearly visible. In addition, we can notice a more pronounced vertical separation above the OH(ν) peak altitudes, which according to von Savigny et al. (2012) is related to the steep vertical gradient in O concentrations and the associated more pronounced collisional deactivation of OH at the upper part of the OH emission layer. By

225 comparison, the vertical shifts between the $\text{OH}(\nu)$ profiles are significantly less pronounced below
the profile peak altitudes.

The systematic increase of the vertical $\text{OH}(\nu)$ shifts above the profile peak altitudes seems to
favour this altitude region for our study on the collisional quenching with O. However, it is important
to keep in mind that any changes in the vertical $\text{OH}(\nu)$ shifts are the convolved response to changes in
230 the quenching and source species concentrations Eq. (2). Therefore, finding the optimum reference
points to compare the vertical shifts between two layers turns out to be less obvious than initially
thought.

Another difficulty arises for the determination of relative peak shifts from the rather coarse vertical
resolution of our simulated OH profiles and observed SABER VER profiles. Despite this constraint
235 on the vertical resolution, we can benefit from the significantly higher dynamic range of the calcu-
lated number densities and observed VERs.

To quantify the vertical $\text{OH}(\nu)$ shifts at the peak altitudes and above, we therefore define two
different reference points, which we determine for each vertical $\text{OH}(\nu)$ profile:

D.1 weighted peak altitude: Zpk_{weighted}

240 In analogy with von Savigny and Lednyts'kyi (2013) we weight the altitudes with the number
density profile $N_{\text{OH}}(\nu, z)$ for each $\text{OH}(\nu)$ layer:

$$Zpk_{\text{weighted}}(\nu) = \frac{\int_0^{\infty} N_{\text{OH}}(\nu, z') z' dz'}{\int_0^{\infty} N_{\text{OH}}(\nu, z') dz'}$$

D.2 shifted peak altitude: $Zpk_{+\text{HWHM}}$

To sense changes between the vertical $\text{OH}(\nu)$ shifts in the upper part of the OH layer, we inter-
245 polate the altitude above the profile peak of each $\text{OH}(\nu)$ layer, where $N_{\text{OH}}(\nu, z)$ has dropped by
a factor of 0.5, i.e. the position that is shifted by the Half Width at Half Maximum (HWHM)
above the profile peak.

For the SABER VER profiles, we can simply replace the number densities by the VERs in the above
250 definitions.

4 Sources of error

While the inclusion of number densities according to D.1 and D.2 helps us to improve the vertical
sensitivity of our model study, systematic departures between simulated and real number densities
are a source of error for our investigation of the collisional quenching effects. The recently published
255 study by Smith et al. (2013) indicates that WACCM tends to underestimate mesospheric ozone con-
centrations, which in turn will impact reaction R1. In addition, WACCM tends to overestimate

mesospheric temperatures according to Smith (2012), which will affect our calculation of the rate constant k_1 and absolute number densities from the SD-WACCM4 temperature pressure fields.

Inspection of Eq. (2) shows that at least a linear departure in the $\text{H} + \text{O}_3$ source profiles from reality is not critical for our analysis, because they will cancel out in the calculation of the $\text{OH}(\nu)$ layer altitudes according to the above stated definitions. The situation is different for the quencher profiles, because any linear scaling of their concentrations cannot be completely factored out in Eq. (2). An overestimation of temperatures should in principle lead to an underestimation of the absolute quenching gas concentrations based on the ideal gas law. In contrast, too high temperatures will lead to an overestimation of the temperature dependent rate constant k_1 . To get an estimate of the associated impact on the vertical shifts between different $\text{OH}(\nu)$ layers, we applied a constant offset of -20 K to our SD-WACCM4 temperatures. Based on this approach, the impact appears to be minor, i.e. in the order of a few tens of meters with regard to our later analysis of profile shifts based on D.1. With respect to the O quenching species the simulated concentrations tend to be lower compared to concentrations derived from SABER as shown in Smith et al. (2011). According to the initial hypothesis on the impact of the collisional quenching with O on the vertical shifts between different $\text{OH}(\nu)$ layers, an underestimated rate of collisional quenching should result in less pronounced vertical shifts. Apart from the discrepancies in simulated O concentrations, the uncertainty of its collisional rate constant k_L^{O} will also affect our results. By comparison with the other quenchers, k_L^{O} has the greatest uncertainty. If we apply the upper and lower boundary of the uncertainty estimates of k_L^{O} from Xu et al. (2012), the changes to the vertical $\text{OH}(\nu)$ shifts based on D.1 range between about 100 m and 160 m with regard to our later analysis.

5 Simulated tidal signatures in OH and O: A monthly case example

Before we will address the temporal variability of vertical $\text{OH}(\nu)$ shifts, we have to reexamine systematic temporal changes of the entire OH emission layer and the O, O_2 quenching species for two reasons: First, we have to make sure that the temporal variability in the SD-WACCM4 data leads to a consistent evolution of the OH and O, O_2 species compared to previous studies. Second, this reexamination helps us to establish an expectation about the impact of temporal changes in the collisional quenching on the vertical $\text{OH}(\nu)$ shifts.

As motivated in the beginning, we will now consider a monthly case example around the September 2010 equinox, where the amplitude of the diurnal migrating tide maximises. For this month, a series of different model results is presented in Fig. 2. The global distribution of the integrated total column of all $\text{OH}(\nu = 1, 2, \dots, 9)$ layers is displayed for 00:00 (UTC) in Panel (a). A general eastward decrease in the integrated OH concentrations is clearly visible. In terms of LSTs, this corresponds to a decrease of integrated OH concentrations over the course of the night. In addition, the OH concentrations are generally high at equatorial latitudes and minimise around $\pm 30^\circ$ lati-

tude, which is consistent with the study of Marsh et al. (2006) and other observational studies stated therein. The steep decrease of integrated OH concentrations at the outer latitudinal and longitudinal margins marks the terminator between day- and nighttime conditions.

295 Weighted OH peak altitudes Zpk_{weighted} according to our previous definition D.1 are displayed in Panel (b). A systematic nighttime increase in the weighted OH peak altitudes by up to 4 km is again clearly visible. Accordingly, we find a significant anti-correlation between OH peak altitudes and concentrations in comparison with Panel (a). Indeed, previous studies based on observations made with the high-resolution Doppler imager (HRDI) instrument and the Wind Imaging Interferometer
300 (WINDII) instrument onboard the upper atmosphere research satellite (UARS) revealed the same coherent anti-correlation between OH peak altitudes and integrated concentrations. Following Liu and Shepherd (2006) and the stated referenced therein, this anti-correlation may be associated to the vertical motions associated with tides or other processes (see also Cho and Shepherd (2006)).

As with the determination of $\text{OH}(\nu)$ profile peak altitudes, several possibilities exist to quantify
305 temporal changes in the quenching species concentrations. The simplest method is to look at the diurnal evolution of a quenching species at a constant height level. However, this method neglects any changes of the quenching species concentrations that arise from the vertical motion of the entire OH layer. To account for this, we may determine the quenching species concentration at a fixed reference point of the OH layer. Again, this method is still rather simple, because the collisional quenching is
310 not constrained to a fixed point at the OH layer. Thus, a more sophisticated approach is to quantify the collisional quenching by weighting the vertical quencher profiles with the corresponding OH profiles (i.e. replace z' in D.1 with the number density $N_Q(z')$ of the quenching species).

For our monthly case example, we applied the latter approach for the O concentrations in Panel (c) of Fig. 2. Accordingly, the equatorial weighted O concentrations show a pronounced maximum
315 before midnight, which has also been confirmed by other observational studies (e.g. see Smith et al. (2010)) and should therefore lead to a pronounced collisional quenching of the OH emission layer at those LSTs. Furthermore, Smith et al. (2010) report another wavenumber 1 type feature at $\pm 30^\circ$ with opposite phase, which at least seems to be reflected at 30°S in our simulations. Of course, we have to bear in mind that we are considering a single month only and that the temporal variability
320 of the OH emission layer is also affecting our weighted O concentrations. Moreover, following the study of Lu et al. (2012) the magnitude of the tidal amplitude seems to be slightly underestimated by WACCM4. Despite this slight underestimation, the tidal signatures in the OH profile weighted O as well as the OH concentrations of our monthly case example show consistent characteristics with previous observations and should therefore serve as a plausible testing ground for the initial
325 hypothesis on the collisional quenching.

If we expand our monthly case example to a full seasonal cycle, we would expect a semi-annual oscillation in the atomic oxygen concentrations, which are following the temporal changes in the amplitude of the diurnal-migrating tide as discussed before. Indeed, this oscillation is clearly visible

in the simulated O concentrations, as shown in the left panel of Fig. 3. For this figure we choose an
 330 LST bin between -1 and 0 hrs around equatorial latitudes. Each curve represents one of the above
 discussed methods to quantify the O concentrations, i.e. O determined at the 0.241 Pa pressure level
 (green line), O interpolated at the selected OH($\nu = 5$) and OH($\nu = 9$) weighted profile peak altitude
 according to our definition D.1 (blue lines), O interpolated at the HWHM shifted position above the
 profile peak (see definition D.2 and red lines), and O weighted with either the selected OH($\nu = 5$)
 335 or OH($\nu = 9$) profile (black lines). Because we are interested in the relative temporal changes in the
 quenching species, each curve is subtracted by its minimum value (see legend) to allow for a better
 intercomparison.

In addition to atomic oxygen, we include the seasonal variability of molecular oxygen in the right
 panel of Fig. 3. Interestingly, we can find another semi-annual oscillation in phase with the atomic
 340 oxygen species, if we consider the curves that do not refer to the fixed 0.241 Pa level. Despite the
 lower quenching efficiency of O₂ compared to O, the higher absolute O₂ abundances will at least
 partially compensate this. Because of the increasing O₂ number density with decreasing altitude,
 the collisional deactivation of excited OH(ν) through O₂ quenching will be most pronounced at the
 lower part of the OH emission layer. Vice versa, the O quenching is rapidly decreasing at the lower
 345 part of the OH emission layer due to the steep vertical gradient in O number densities, thus, O₂
 quenching is expected to be the dominant process of vibrational deactivation of OH at the bottom of
 the OH emission layer. This already seems to indicate an important role of the seasonality in the O₂
 quenching with regard to the temporal evolution of vertical OH(ν) shifts.

6 Seasonal evolution of OH layer shifts

350 6.1 Sensitivity study

In the following, we will compare relative changes in the vertical shifts between the OH($\nu = 9$)
 and OH($\nu = 5$) profiles. We select these two vibrational states because each of them contributes to
 emissions, which can be observed by either the 1.6 μm or 2.0 μm SABER channel. Ideally, one
 must consider that each SABER channel captures a mixture of emissions that belong to two different
 355 transition bands. However, because the difference in vibrational levels between each transmission
 is limited to $\Delta\nu = 1$, we assume that we can neglect the effect of profile mixing for each channel,
 if we are interested in the relative vertical shift between both (mixed) OH profiles. The vertical
 shift between a simulated OH($\nu = 9$) and OH($\nu = 5$) profile will be calculated from the difference
 between either their weighted peak altitudes:

$$360 \Delta Zpk_{\text{weighted}} = Zpk_{\text{weighted}}[\text{OH}(\nu = 9)] - Zpk_{\text{weighted}}[\text{OH}(\nu = 5)], \quad (3)$$

or from the difference between the HWHM shifted altitudes above the profile peaks:

$$\Delta Zpk_{+\text{HWHM}} = Zpk_{+\text{HWHM}}[\text{OH}(\nu = 9)] - Zpk_{+\text{HWHM}}[\text{OH}(\nu = 5)]. \quad (4)$$

The vertical shifts between the SABER 1.6 μm and 2.0 μm VER profiles are determined in the same way.

365 We will now investigate the seasonal variability of the relative vertical shifts between our simulated $\text{OH}(\nu = 9)$ and $\text{OH}(\nu = 5)$ profiles, which we denote as $\text{OH}(9;5)$ profile shifts in the following. For this task, we perform three different model runs:

- all quenching species are activated
- O quenching species is deactivated
- 370 – O_2 quenching species is deactivated

This allows us to study the impact of collisional quenching on the $\text{OH}(9;5)$ profile shifts for both species.

The results from our three model runs are shown in Fig. 4. Panel (a) displays the seasonal evolution of $\text{OH}(9;5)$ profile shifts for the first model run (i.e. complete quenching considered). The 375 left axis/solid line refer to the relative vertical shifts between weighted peak altitudes according to Eq. (3). The right/dashed line refer to the relative vertical shifts at the upper part of the $\text{OH}(9;5)$ layers according to Eq. (4). If we concentrate on the solid line first, we find indeed a semi-annual oscillation in the $\text{OH}(9;5)$ profile shifts that is in phase with the observed changes in the O and O_2 concentrations according to Fig. 3. On the other hand, if we look at the upper part of the $\text{OH}(9;5)$ 380 layers (dashed line), the fluctuations in the seasonal variability are much more pronounced and the response to the seasonal changes in the quenching species is less clear. So far, we find the best agreement with the initial hypothesis on the collisional quenching process for our weighted peak altitude definition D.1.

Similar to Panel (a), Panel (b) shows the model run with the deactivated O quenching process. For 385 both lines, we find a significant decrease in the $\text{OH}(9;5)$ profile shifts, which again is consistent with the initial hypothesis. On the other hand, we still find a persisting semi-annual oscillation for the solid line (i.e. $\text{OH}(9;5)$ profile shifts with respect to weighted peak altitudes) that is superimposed by another temporal maximum around mid January 2010. The seasonal response at the upper part of the $\text{OH}(9;5)$ layers (dashed line) remains less clear. If we now subtract the results from the 390 model runs with and without O quenching, we find a clear semi-annual response in the $\text{OH}(9;5)$ profile shifts according to the solid line in Panel (c). Interestingly, if we compare the increase in the $\text{OH}(9;5)$ profile shifts between July and October between Panel (b) and (c), the contribution of the O quenching process to the temporal changes in the $\text{OH}(9;5)$ profile shifts is just slightly above the remaining temporal changes for the model run with deactivated O quenching. With regard to the 395 initial hypothesis, this suggests that we cannot address the observed seasonality in $\text{OH}(9;5)$ profile shifts to the modulation in the collisional O quenching only.

We therefore repeat the same investigation of the collisional quenching process for the O_2 quencher. In analogy with Panel (c), Panel (d) shows the difference in $\text{OH}(9;5)$ profile shifts when subtracting

the results from the model runs with activated and deactivated O₂ quenching. Again, the upper part
400 of the OH(9;5) layers shows strong fluctuations (dashed lines), thus we will limited our discussion
to the relative shifts between weighted peak altitudes (solid line). First of all, we find that the de-
activation of the O₂ quenching in our model run leads to a still noticeable decrease in the vertical
OH(9;5) profile shifts. If we neglect the maximum around January 2011, we can find a further semi-
annual response in the vertical OH(9;5) profile shifts due to the switching between the deactivated
405 and activated O₂ quenching. In comparison with the seasonal change in the OH(9;5) profile shifts
between July and October due to the deactivation of the O quenching (see panel c), the impact of the
deactivation of O₂ quenching is less than one half.

With respect to the model run that considers all quenching species (see Panel a), we notice that
simply adding the effect of O and O₂ quenching according to Panel (c,d) still leads to considerably
410 smaller vertical OH(9;5) profile shifts, as shown in Panel (d). On the other hand, the agreement
in the seasonal variability between Panel (a) and (d) is quite good. This becomes evident, if we
determine the best scaling factor between both functions in a least-squares sense. Accordingly, the
grey line in Panel (d) denotes the $\Delta Zpk_{\text{weighted}}$ profile shift values from Panel (a) divided by 1.438.
Apparently, taking the sum of Panel (c,d) leads to an improved agreement in the seasonal variability
415 with respect to Panel (a) rather than considering the effect of deactivating either O or O₂ quenching
only. This again suggests the importance of the O₂ quenching to the seasonal variability. Still, the
question remains, why the sum of Panel (c,d) is smaller by a factor of 1.438 compared to the complete
quenching model run in Panel (a). As noticed before, the impact of N₂ quenching is insufficient to
serve as an explanation, i.e. it leads to a difference between 40 m to 50 m, if we subtract a model
420 run with deactivated N₂ quenching from the complete quenching case in Panel (a) (not shown). This
indicates that the combined effect of O and O₂ quenching is larger than the sum of their individual
contributions.

As discussed in the beginning, seasonal changes in the vertical H+O₃ profiles will affect the OH
emission layer width, which in turn will also affect the OH(9;5) profile shifts. In addition to the
425 combined effect of O and O₂ quenching, this could provide another mechanism that is driving the
temporal variability. The seasonal evolution of the OH emission layer width is shown in Panel (f) of
Fig. 4. In this case, we determine the width of the vertical profile by the Full Width at Half Maximum
(FWHM) to account for changes above and below the profile peak altitude. Accordingly, we find
a pronounced increase around the mid of January 2011 in the FWHM values, which is coherent
430 with the observed additional increase in the OH(9;5) profile shifts for the deactivated O quenching
case (Panel b). This gives an explanation, why the drop in the vertical OH(9;5) profile shifts is less
pronounced after the winter solstice according to Panel (a). Furthermore, the larger extent of the OH
profile width may also favour the rate of collisional O₂ quenching, which could explain the coherent
response according to Panel (d) of Fig. 4. On the other hand, a coherent semi-annual variability
435 with respect to the $\Delta Zpk_{\text{weighted}}$ profile shift values in Panel (a) is not evident, which strengthens the

argument of the combined effect of O and O₂ quenching as the dominant driving mechanism of the seasonal variability in the OH(9;5) profile shifts.

Finally, we also consider the relative changes of the OH(9) and OH(5) peak widths, which should particularly influence the OH(9;5) profile shifts above the profile peak altitudes. The seasonal evolution of each peak width is shown by the grey lines in Panel (g) of Fig. 4 (see caption). The difference we receive by subtracting both temporal evolutions with each other is shown by the black solid line. We find that the large relative changes in the profile widths around October 2010 and May 2011 are coherent with the observed jumps in the OH(9;5) profile shifts at the upper part of the OH(9;5) layers (see dashed line in Fig. 4a), i.e. the vertical shifts $\Delta Z_{pk+HWHM}$ appear to react more sensitively to relative changes in the OH(9;5) profile widths.

6.2 Comparison with SABER

We will now focus on the seasonal variability of the vertical shifts between the SABER 1.6 and 2.0 μm VER profiles for the period from January 2009 to December 2011. In analogy with our sensitivity study, we choose the same -1 h to 0 h LST bin for the results presented in Fig. 5. Here, each point represents the mean value based on three matching yaw-cycles between 2009 to 2011. Each error bar denotes the corresponding standard deviation. Panel (a-b) show the seasonal variability in the VER profile shifts for two equatorial latitude bins. Again, the solid line refers to the vertical shifts between weighted peak altitudes according to Eq. 3 (left axis) and the dashed line refers to the vertical shifts at the upper part of the VER profiles according to Eq. 3 (right axis). The seasonal variability of derived O concentrations is displayed in Panel (c-d). The black line shows the O concentrations at 90 km altitude (left axis). The grey dotted and dashed lines show the VER profile weighted O concentrations with respect to the 1.6 μm and 2.0 μm channel (right axis). Panel (e-f) show the seasonal variability of the 1.6 and 2.0 μm VER profile widths (dashed and dotted, left axis) as well as their relative difference (black solid line, right axis).

First of all, we notice that a semi-annual oscillation - with maxima around May and October - is also present in the SABER VER profile shifts. Indeed, we find another coherent semi-annual oscillation in the O concentrations for the 0° to 10° S bin. With regard to the 0° to 10° N bin a faint semi-annual structure is present, but the overall change is dominated by an annual oscillation. Interestingly, in comparison with the changes in the SABER VER profile shifts, the semi-annual response is more dominating in the 10° N rather than the 10° S latitude bin. Again, this indicates that the consideration of O quenching alone cannot sufficiently explain the seasonal variability of SABER VER profile shifts. In contrast to our model results, we cannot directly rule out that changes in the sources gases may significantly affect the seasonality of the observed VER profile shifts, because of the limited spectral bandwidth of SABER, which prevents us from sensing all Meinel bands of the OH emission.

If we consider the relative changes of the VER profile widths according to the black solid line in

Panel (e-f) of Fig. 5, we can find a similar coherent response in the vertical shifts at the upper part of both VER profiles (see dashed line in panel a-b), which again shows the stronger sensitivity of this profile shift definition to changes in the relative profile shapes.

475 7 Diurnal evolution of OH layer shifts

7.1 Sensitivity study

In analogy with our analysis of the seasonal variability of the vertical OH(9;5) profile shifts in the previous section, we perform the same three model runs where we consider the full-quenching case, the deactivation of O quenching and the deactivation of O₂ quenching. To improve our later
480 comparison with the observed diurnal variability from SABER, we adjust the temporal averaging period in our model runs to the same period that is required for a full SABER yaw cycle.

Accordingly, Fig. 6 shows the diurnal variability of both simulated quenching species around the September 2010 equinox at equatorial latitudes, where the amplitude of the diurnal migrating tide maximises. Again, we use the same definitions to quantify changes in the O and O₂ concentrations
485 as in Fig. 3.

While the different definitions of O concentrations only lead to a slight phase shift in the temporal evolution of the O concentrations of up to one hour, the different definitions of O₂ concentrations can result in quite different diurnal evolutions. With regard to the systematic increase in the nighttime OH peak altitudes (Fig. 2b), the decrease in the OH profile weighted O₂ concentrations (black lines)
490 and interpolated O₂ concentrations at the weighted OH peak altitude (blue lines) appears to be the most consistent.

The results from our three model runs are shown in Fig. 7, with the solid lines (left axis) referring to the OH(9;5) profile shift according to Eq. (3) and the dashed lines (right axis) referring to Eq. (4) correspondingly. Panel (a) displays the peak shifts for the first model run, which considers all
495 quenching species. Panel (b) shows the OH(9;5) profile shifts for the model run with deactivated O quenching. Panel(c-d) show the difference in OH(9;5) profile shifts, if we subtract either the model run with deactivated O or O₂ quenching from the full quenching model run shown in Panel (a). Similar to the previous section, we also include the sum of Panel (c,d) in Panel (e).

Keeping in mind the initial hypothesis on the effect of collisional quenching, we would expect
500 that the vertical OH(9;5) profile shifts should maximise shortly before midnight according to the maximising O concentrations. However, neither of both OH(9;5) profile shift definitions matches with this expectation according to Panel (a). Furthermore, we notice that the diurnal variability in the OH(9;5) profile shift is rather opposite for both definitions. If we switch off the O quenching according to our second model run (Panel b), the vertical OH(9;5) profile shifts are significantly
505 reduced as it was also the case for our investigation of the seasonal variability in Fig. 4b. Moreover, if we consider the impact of the collisional O quenching according to Panel (c), a coherent response

to the diurnal evolution of O is clearly visible for the $\Delta Zpk_{\text{weighted}}$ values (solid line). For the HWHM shifted positions above the profile peaks (dashed line), we can still find a significant internal variability, such that the impact of collisional O quenching again remains less clear.

510 As with our analysis of the seasonal variability, the collisional O₂ quenching is also significantly affecting the vertical OH(9;5) profile shifts according to Panel (d) of Fig. 7. In comparison with the collisional O quenching the effect is still smaller with regard to the weighted peak altitudes. Furthermore, the relative changes due to the deactivation of O₂ quenching remain rather constant after -2 hrs. In contrast, if we consider the results based on the HWHM shifted locations, the effect
515 of the deactivation of O₂ quenching strongly exceeds the corresponding effect for O. Moreover, the early $Zpk_{\text{weighted}}[\text{OH}(5)]$ positions are even higher than those of the $Zpk_{\text{weighted}}[\text{OH}(9)]$ positions, which leads to the negative values before -3 hrs.

If we consider the sum of Panel (c,d), as shown in Panel (e), the resulting OH(9;5) profile shifts are again significantly smaller compared to the model run in Panel (a) which considers all quenching
520 species simultaneously. Interestingly, if we search for the best scaling factor between both panels, we obtain a factor of 1.430, which is very close to the scaling factor we receive for the seasonal variability. On the other hand, the agreement between the diurnal evolution according to the sum of Panel (c,d) and the scaled Panel (a), which is denoted by the grey line in Panel (e), is less clear for the early evening hours. During the same hours, we notice a strong shrinking of the entire OH
525 emission layer by up to 4 km due to the nighttime evolution of the H+O₃ source gases according to Fig. 8a. This may also provide an explanation for the departure between the sum of Panel (c,d) and scaled Panel (a), presuming that the combined effect of O and O₂ quenching can be described by its linearly scaled sum according to Fig. 7. With regard to the OH(9;5) profile shifts based on $\Delta Zpk_{+\text{HWHM}}$ values (dashed lines), we find that these are again strongly correlated with the relative
530 changes in the OH(9,5) profile widths according to Fig. 8b.

We expand our analysis to the full year of simulated OH(ν) populations and summarise the found correlations between vertical OH(9;5) profile shifts and quenching species concentrations in Fig. 9 and Fig. 10. Following the displayed correlation plots in Fig. 9, we find no significant correlation between the vertical OH(9;5) profile shifts and weighted OH(9) concentrations for all seasons and
535 both peak shift definitions. A weak positive correlation is only visible, if we include all data points in Panel (a). As with our equinoctial case example according to Fig. 7c, the correlation between vertical OH(9;5) profile shifts and weighted O concentrations significantly improves, if we compare the relative changes between the model runs with activated and deactivated O quenching for weighted peak altitudes (Fig. 9c). In contrast, the correlation remains poor, if we consider OH(9;5) profile
540 shifts at the upper part of both layers (Fig. 9d).

Figure 10 shows the corresponding correlations for the O₂ quencher. In contrast to the O quencher, the correlations with the vertical OH(9;5) profile shifts are exceptionally high. Of course we have to bear in mind that the systematic increase in the OH nighttime altitudes (see Fig. 2b) will also

be reflected in the systematic decrease in OH(9) weighted O₂ concentrations. However, for the
545 relative changes between the model runs with activated and deactivated O₂ quenching, we still find
a significant correlation in Panel (c), respectively anti-correlation in Panel (d) of Fig. 10.

In summary, the nighttime evolution in the OH(9;5) profile shifts can hardly be explained by
the process of collisional quenching with atomic oxygen only. Again, the inclusion of molecular
oxygen quenching further improves the correlation with the OH(9;5) profile shifts. In addition, the
550 simultaneous strong decrease of the entire OH layer width, driven by the H+O₃ source profiles, will
further impact the nighttime evolution of OH(9;5) profile shifts. Interestingly, the systematic changes
in OH peak altitudes and associated changes in O₂ concentrations show a very strong correlation
with the temporal changes in the vertical OH(9;5) profile shifts.

7.2 Observed diurnal variability from SABER

555 For the SABER observations we first consider the same yaw-cycle that was also used for the model
simulations presented in Fig. 7 and compare the relative shifts between the 1.6 μm and 2.0 μm VER
profiles with the OH-VER weighted atomic oxygen profiles similar to our analysis on the seasonal
variability. For the observed diurnal variability, it is important to note that the temporal evolution
in the observed relative OH profile shifts may significantly differ from our model results because of
560 the existence of additional non-migrating tides as being reported by Xu et al. (2010) from SABER
observations at lower latitudes. These tides would complicate a direct comparison with our model
results, since we have to extract the temporal evolution from the longitudinal variability of our 00:00
UTC model outputs. However, despite the possible existence of non-migrating tides, this does not
prevent us from testing the hypothesis on the impact of collisional quenching with regard to the
565 temporal variability of the O quenching species.

In analogy with Fig. 7 the SABER results are shown in Fig. 11 for the same yaw-cycle and for
two latitudinal bins nearby the equator. Indeed, the nighttime evolution of relative OH profile shifts
looks quite different compared to our modelled vertical OH(9,5) profile shifts. Furthermore, the
amplification of atomic oxygen before midnight is not as evident as in our model results. Despite
570 these discrepancies, we would expect from the systematic nighttime decrease in atomic oxygen
a corresponding feedback in the vertical VER peak shifts, which clearly is not the case. Again, we
also notice strong changes in the relative peak widths according to Panel (e) and (f) of Fig. 7 that are
partially reflected in the nighttime changes of VER peak shifts.

If we expand our analysis to a full seasonal cycle, the missing correlation between VER profile
575 shifts and O concentrations remains. Accordingly, the process of collisional O quenching appears
to be insufficient to explain the nighttime evolution of the OH VER profile shifts, which also agrees
with our model expectations in a qualitative sense.

8 Summary and Conclusion

Following the hypothesis that the process of collisional quenching is significantly affecting the vertical shifts between different OH(ν) layers, this study investigated the impact of the temporal variability of the collisional quenching on the seasonal as well as the diurnal evolution of the vertical shifts between the OH(9) and OH(5) layer. This was done by establishing an updated quenching model, which uses the model output from a state-of-the-art 3D chemical climate model (SD-WACCM4) to simulate the temporal variability of both OH(ν) layers.

By comparing different model runs, which consider either all quenching species or neglect the collisional quenching process by O or O₂, we could study the actual impact of the temporal variability of O and O₂ quenching on the vertical OH(9;5) profile shifts. For the seasonal variability we find that both quencher have a noticeable impact on the vertical OH(9;5) profile shifts, which manifests in a semi-annual variability that is following the temporal evolution of the diurnal migrating tide at the equator. Furthermore, the simultaneous quenching of both species results in about 1.4x larger vertical OH(9;5) profile shifts than we would receive from the sum of their individual contributions. With regard to previous studies that were mainly focusing on the effect of collisional quenching with O, this indicates the important role of the combined effects of O and O₂ quenching on the vertical structure of the OH layer. In addition, the strong change in the OH emission layer widths around January 2011 demonstrates that temporal changes in the H+O₃ profiles provide another mechanism to affect the OH(9;5) profile shifts.

We found further evidence of the same seasonality in the OH(9;5) profile shifts in the SABER observations, even though the coherence with changes in the derived SABER O concentrations is not always as clearly pronounced as it is the case in our model simulations. This could reflect the stronger temporal variability in the true H+O₃ profiles, which is competing with the temporal changes in the collisional quenching processes.

With regard to the diurnal variability our model study as well as our analysis of SABER VER profiles clearly show that the collisional quenching process of OH with O is insufficient to describe the temporal evolution alone. Again, the consideration of the combined effect of O and O₂ quenching is required to describe the temporal shifts in the OH(9;5) profiles. In addition, the model results suggest that the nighttime evolution of the H+O₃ profiles is significantly affecting the vertical OH(9;5) profile shifts for the first half of the night.

In summary, according to this study the effect of the collisional quenching does have a noticeable impact on the temporal variability of OH(9;5) profile shifts at the equator, but requires the simultaneous consideration of the O and O₂ quenching species to provide a proper description of the observed temporal evolution. While the O and O₂ quenching appears to be modulated in phase with regard to their seasonal evolution, the need of the simultaneous consideration of both quenching species becomes even more important for the diurnal evolution, where the modulation of O and O₂ can differ substantially, such that we cannot find a meaningful correlation to changes in the O quenching

615 alone.

Because of the manifold of transition bands being observed by different ground-based instruments, a thorough understanding of the driving processes of the variability of OH emission altitudes is crucial for the intercomparison and interpretation of long-term data sets. This in particular applies for studying of mesopause temperature trends by means of OH rotational temperature measurements
620 (see Beig et al. (2003); Beig (2011) for a comprehensive review on this topic). Further improvements in the modelling of the tidal variability at the mesopause as well as the inclusion of a multiyear analysis of the features that have been discussed here would further contribute to a better quantitative understanding of the systematic biases between different observational long-term studies.

625 *Acknowledgements.* This work was in part supported by Ernst-Moritz-Arndt-University of Greifswald. Further support was granted by the German Research Foundation (Deutsche Forschungsgemeinschaft, DFG) under project PA 1714/4-2. We thank R. R. Garcia and D. E. Kinnison, NCAR Boulder, for providing the SD-WACCM4 data to us, which have been a crucial component of this study. In addition, we thank C. Hoffman, former member of the IUP Bremen and A. K. Smith, NCAR Boulder, for the helpful discussions on the SD-
630 WACCM4 data and the employed quenching model to this study. Finally, we are indebted to the SABER team for making SABER data available.

References

- Adler-Golden, S.: Kinetic parameters for OH nightglow modeling consistent with recent laboratory measurements, *J. Geophys. Res.*, 102, 19 969–19 976, doi:10.1029/97JA01622, 1997.
- 635 Baker, D. J. and Stair Jr, A. T.: Rocket measurements of the altitude distributions of the hydroxyl airglow, *Physica Scripta*, 37, 611–, doi:10.1088/0031-8949/37/4/021, 1988.
- Bates, D. R. and Nicolet, M.: The photochemistry of atmospheric water vapor, *J. Geophys. Res.*, 55, 301–327, doi:10.1029/JZ055i003p00301, 1950.
- Beig, G.: Long-term trends in the temperature of the mesosphere/lower thermosphere region: 2. Solar response, *J. Geophys. Res.*, 116, A00H12–, doi:10.1029/2011JA016766, 2011.
- 640 Beig, G., Keckhut, P., Lowe, R. P., Roble, R. G., Mlynczak, M. G., Scheer, J., Fomichev, V. I., Offermann, D., French, W. J. R., Shepherd, M. G., Semenov, A. I., Remsberg, E. E., She, C. Y., Lübken, F. J., Bremer, J., Clemesha, B. R., Stegman, J., Sigernes, F., and Fadnavis, S.: Review of mesospheric temperature trends, *Rev. Geophys.*, 41, 1015–, doi:10.1029/2002RG000121, 2003.
- 645 Cho, Y.-M. and Shepherd, G.: Correlation of airglow temperature and emission rate at Resolute Bay (74.86°N), over four winters (2001–2005), *Geophys. Res. Lett.*, 33, L06 815–, doi:10.1029/2005GL025298, 2006.
- Cogger, L. L., Elphinstone, R. D., and Murphree, J. S.: Temporal and latitudinal 5577 Å airglow variations, *Can. J. Phys.*, 59, 1296–1307, doi:10.1139/p81-170, 1981.
- Dodd, J. A., Lipson, S. J., Lowell, J. R., Armstrong, P. S., Blumberg, W. A. M., Nadile, R. M., Adler-Golden, S. M., Marinelli, W. J., Holtzclaw, K. W., and Green, B. D.: Analysis of hydroxyl earthlimb airglow emissions: Kinetic model for state-to-state dynamics of OH (ν ,N), *J. Geophys. Res.*, 99, 3559–3585, doi:10.1029/93JD03338, 1994.
- 650 Garcia, R. R., Marsh, D. R., Kinnison, D. E., Boville, B. A., and Sassi, F.: Simulation of secular trends in the middle atmosphere, 1950;2003, *J. Geophys. Res.*, 112, D09 301–, doi:10.1029/2006JD007485, 2007.
- 655 Hoffmann, C. G., Kinnison, D. E., Garcia, R. R., Palm, M., Notholt, J., Raffalski, U., and Hochschild, G.: CO at 40–80 km above Kiruna observed by the ground-based microwave radiometer KIMRA and simulated by the Whole Atmosphere Community Climate Model, *Atmos. Chem. Phys.*, 12, 3261–3271, doi:10.5194/acp-12-3261-2012, 2012.
- Khomich, V., Semenov, A., and Shefov, N.: Airglow as an Indicator of Upper Atmospheric Structure and Dynamics, Springer Berlin Heidelberg, doi:10.1007/978-3-540-75833-4, 2008.
- 660 Krassovsky, V. I.: Chemistry of the upper atmosphere, *Space Res.*, 3, 96–116, 1963.
- Liu, G. and Shepherd, G. G.: An empirical model for the altitude of the OH nightglow emission, *Geophys. Res. Lett.*, 33, L09 805–, doi:10.1029/2005GL025297, 2006.
- Lu, X., Liu, H.-L. L., Liu, A. Z., Yue, J.M. McInerney, J. M., and Z, L.: Momentum budget of the migrating diurnal tide in the Whole Atmosphere Community Climate Model at vernal equinox, *J. Geophys. Res.*, 117, D07 112, doi:10.1029/2011JD017089, 2012.
- 665 Makhlof, U. B., Picard, R. H., and Winick, J. R.: Photochemical-dynamical modeling of the measured response of airglow to gravity waves 1. Basic model for OH airglow, *J. Geophys. Res.*, 100, 11 289–11 311, doi:10.1029/94JD03327, 1995.
- 670 Marsh, D. R., Smith, A. K., Mlynczak, M. G., and Russell, J. M.: SABER observations of the OH Meinel airglow variability near the mesopause, *J. Geophys. Res.*, 111, A10S05–, doi:10.1029/2005JA011451, 2006.

- McDade, I. C.: The altitude dependence of the OH($X^2\Pi$) vibrational distribution in the nightglow: Some model expectations, *Planetary and Space Science*, 39, 1049–1057, doi:10.1016/0032-0633(91)90112-N, 1991.
- McDade, I. C. and Llewellyn, E. J.: Mesospheric oxygen atom densities inferred from night-time OH Meinel
675 band emission rates, *Planetary and Space Science*, 36, 897–905, doi:10.1016/0032-0633(88)90097-9, 1988.
- Mertens, C. J., Russell III, J. M., Mlynczak, M. G., She, C.-Y., Schmidlin, F. J., Goldberg, R. A., López-Puertas, M., Wintersteiner, P. P., Picard, R. H., Winick, J. R., and Xu, X.: Kinetic temperature and carbon dioxide from broadband infrared limb emission measurements taken from the TIMED/SABER instrument, *Adv. Space. Res.*, 43, 15–27, doi:10.1016/j.asr.2008.04.017, 2009.
- 680 Mlynczak, M. G., Hunt, L. A., Mast, J. C., Thomas Marshall, B., Russell, J. M., Smith, A. K., Siskind, D. E., Yee, J.-H., Mertens, C. J., Javier Martin-Torres, F., Earl Thompson, R., Drob, D. P., and Gordley, L. L.: Atomic oxygen in the mesosphere and lower thermosphere derived from SABER: Algorithm theoretical basis and measurement uncertainty, *J. Geophys. Res. Atmos.*, 118, 5724–5735, doi:10.1002/jgrd.50401, 2013.
- Rothman, L., Gordon, I., Barbe, A., Benner, D., Bernath, P., Birk, M., Boudon, V., Brown, L., Campargue, A.,
685 Champion, J.-P., Chance, K., Coudert, L., Dana, V., Devi, V., Fally, S., Flaud, J.-M., Gamache, R., Goldman, A., Jacquemart, D., Kleiner, I., Lacome, N., Lafferty, W., Mandin, J.-Y., Massie, S., Mikhailenko, S., Miller, C., Moazzen-Ahmadi, N., Naumenko, O., Nikitin, A., Orphal, J., Perevalov, V., Perrin, A., Predoi-Cross, A., Rinsland, C., Rotger, M., Šimečková, M., Smith, M., Sung, K., Tashkun, S., Tennyson, J., Toth, R., Vandaele, A., and Vander Auwera, J.: The HITRAN 2008 molecular spectroscopic database, *JQSRT*, 110,
690 533–572, doi:10.1016/j.jqsrt.2009.02.013, 2009.
- Russell III, J. M., Mlynczak, M. G., Gordley, L. L., Tansock, Jr., J. J., and Esplin, R. W.: Overview of the SABER experiment and preliminary calibration results, in: *Society of Photo-Optical Instrumentation Engineers (SPIE) Conference Series*, edited by Larar, A. M., vol. 3756 of *Society of Photo-Optical Instrumentation Engineers (SPIE) Conference Series*, pp. 277–288, doi:10.1117/12.366382, 1999.
- 695 Sander, S. P., Abbatt, J., Barker, J. R., Burkholder, J. B., Friedl, R. R., Golden, D. M., Huie, R. E., Kolb, C. E., Kurylo, M. J., Moortgat, G. K., Orkin, V. L., and Wine, P. H.: *Chemical Kinetics and Photochemical Data for Use in Atmospheric Studies*, Evaluation No. 17, JPL Publication, Jet Propulsion Laboratory, Pasadena, 10-66, 1–12, 2011.
- Shepherd, M. G., Liu, G., and Shepherd, G. G.: Mesospheric semiannual oscillation in temperature and night-
700 glow emission, *Journal of Atmospheric and Solar-Terrestrial Physics*, 68, 379–389, doi:10.1016/j.jastp.2005.02.029, 2006.
- Smith, A. K.: Global dynamics of the MLT, *Surv Geophys*, 33, 1177–1230–, doi:10.1007/s10712-012-9196-9, 2012.
- Smith, A. K., Marsh, D. R., Mlynczak, M. G., and Mast, J. C.: Temporal variations of atomic oxygen in the
705 upper mesosphere from SABER, *J. Geophys. Res.*, 115, D18 309–, doi:10.1029/2009JD013434, 2010.
- Smith, A. K., Garcia, R. R., Marsh, D. R., and Richter, J. H.: WACCM simulations of the mean circulation and trace species transport in the winter mesosphere, *J. Geophys. Res.*, 116, D20 115–, doi: 10.1029/2011JD016083, 2011.
- Smith, A. K., Harvey, V. L., Mlynczak, M. G., Funke, B., García-Comas, M., Hervig, M., Kaufmann, M.,
710 Kyrölä, E., López-Puertas, M., McDade, I., Randall, C. E., Russell, J. M., Sheese, P. E., Shiotani, M., Skinner, W. R., Suzuki, M., and Walker, K. A.: Satellite observations of ozone in the upper mesosphere, *J.*

- Geophys. Res. Atmos., 118, 5803–5821, doi:10.1002/jgrd.50445, 2013.
- Steinfeld, J. I., Adler-Golden, S. M., and Gallagher, J. W.: Critical survey of data on the spectroscopy and kinetics of ozone in the mesosphere and thermosphere, Phys. Chem. Ref. Data, 16, 911–951, doi:10.1063/1.555796, 1987.
- 715 von Savigny, C. and Lednyts'kyi, O.: On the relationship between atomic oxygen and vertical shifts between OH Meinel bands originating from different vibrational levels., Geophys. Res. Lett., n/a, n/a–n/a, doi:10.1002/2013GL058017, 2013.
- 720 von Savigny, C., McDade, I. C., Eichmann, K.-U., and Burrows, J. P.: On the dependence of the OH* Meinel emission altitude on vibrational level: SCIAMACHY observations and model simulations, Atmos. Chem. Phys., 12, 8813–8828, doi:10.5194/acp-12-8813-2012, 2012.
- Xu, J., Smith, A. K., Jiang, G., Gao, H., Wei, Y., Mlynczak, M. G., and Russell, J. M.: Strong longitudinal variations in the OH nightglow, Geophys. Res. Lett., 37, L21 801–, doi:10.1029/2010GL043972, 2010.
- 725 Xu, J., Gao, H., Smith, A. K., and Zhu, Y.: Using TIMED/SABER nightglow observations to investigate hydroxyl emission mechanisms in the mesopause region, J. Geophys. Res., 117, D02 301–, doi:10.1029/2010GL043972, 2012.
- Yee, J.-H., Crowley, G., Roble, R. G., Skinner, W. R., Burrage, M. D., and Hays, P. B.: Global simulations and observations of O(¹S), O₂(¹Σ) and OH mesospheric nightglow emissions, J. Geophys. Res., 102, 19 949–19 968, doi:10.1029/96JA01833, 1997.

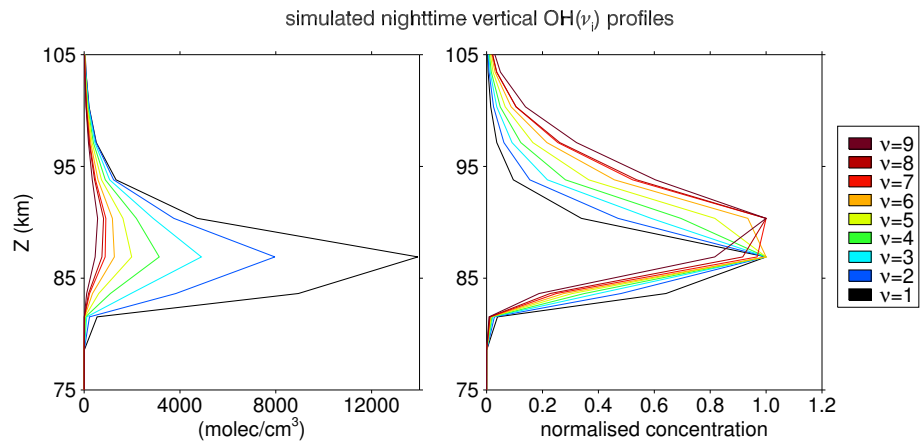


Fig. 1: Vertical OH(ν) profiles calculated from monthly averaged SD-WACCM4 model output for September 2010, 00:00 UTC at the 0° equatorial latitude. Left panel: absolute number concentrations. Right panel: normalised OH(ν) profiles.

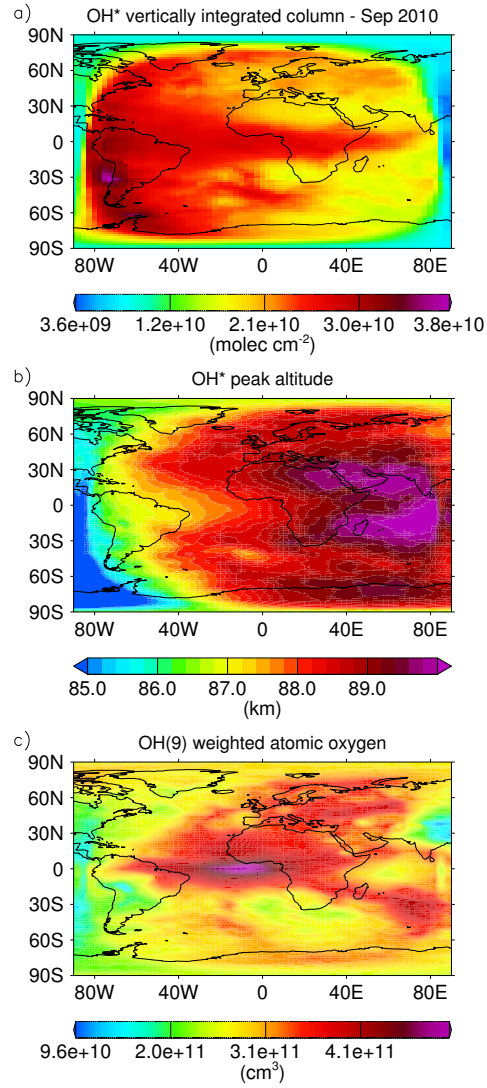


Fig. 2: Monthly averaged model results around September 2010 equinox. Panel (a): Vertically integrated number density of simulated $\sum_{i=1}^9 \text{OH}(\nu_i)$. Panel (b): Weighted peak altitudes of simulated OH emission layer according to our definition D.1. Panel (c): O concentration weighted with the OH emission layer.

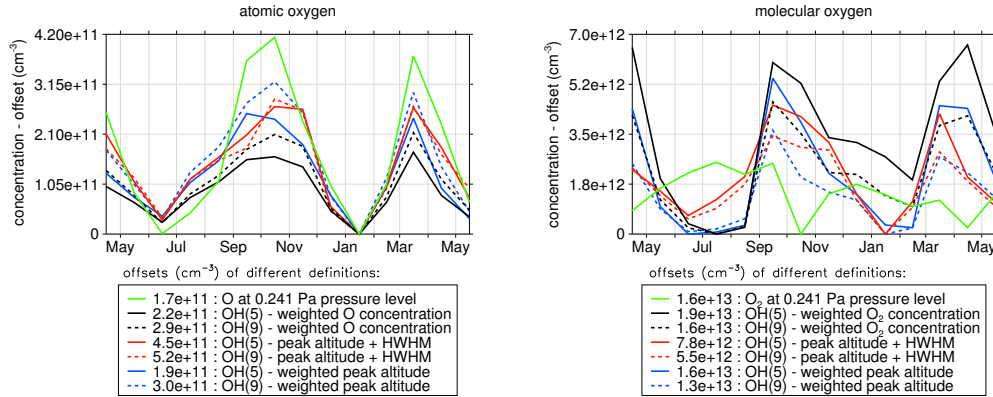


Fig. 3: Seasonal variability of simulated atomic and molecular oxygen concentrations from April 2010 to June 2011 according to the following definitions: O concentration at fixed pressure level (green line), O concentration interpolated at +HWHM shifted and weighted peak altitudes (red and blue lines), O concentration weighted with OH concentrations (black lines). From each curve the offsets listed in the legend were subtracted to allow a better intercomparison of the temporal changes.

constant	reference	remark
P	Adler-Golden (1997)	based on values from Steinfeld et al. (1987)
A	Xu et al. (2012)	values based on Hitran database (Rothman et al., 2009)
$k_3^{O_2}; \alpha$	Adler-Golden (1997)	based on table 2 ; α = correction factor from Xu et al. (2012)
$k_l^{N_2}$	Adler-Golden (1997)	taken from table 1
$k_l^O; \beta$	Smith et al. (2010)	β = correction factor from Xu et al. (2012)
k_1	Sander et al. (2011)	SD-WACCM4 temperatures used for calculation of k_1

Table 1: Employed constants to Eq.(2)

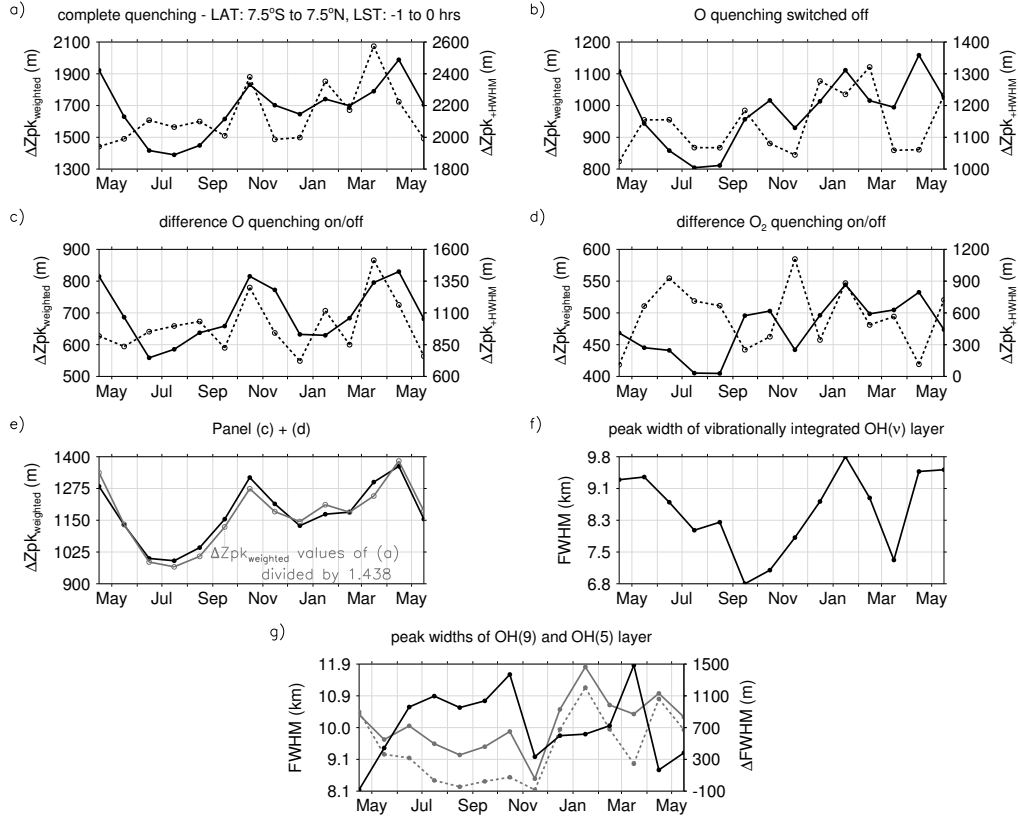


Fig. 4: Panel (a-d): Seasonal variability of vertical OH(9;5) profile shifts from April 2010 to June 2011 for different model runs within the equatorial range between $\pm 7.5^\circ$ and the LST range from -1 to 0 hrs. Solid line/left axis: OH(9;5) vertical shifts between weighted peak altitudes (see definition D.1). Dashed line/right axis: OH(9;5) vertical shifts between the +HWHM shifted peak positions (see definition D.2). Panel(a): Full quenching model run. Panel(b): Deactivated O quenching model run. Panel(c): Difference in peak shifts when switching O quenching on/off. Panel(d): Difference in peak shifts when switching O₂ quenching on/off. Panel (e): {Panel (c) + (d)} (black line). In addition, $\Delta Zpk_{weighted}$ from Panel (a) divided by 1.438 shown by grey line. Panel(f): Full peak width of the vibrationally integrated OH(ν) layer. Panel (f)/left axis: Full peak widths of OH(9) and OH(5) layers (dashed and solid grey lines). Panel (g)/right axis: Relative difference between the full peak widths of the OH(9) and OH(5) layers (black solid line).

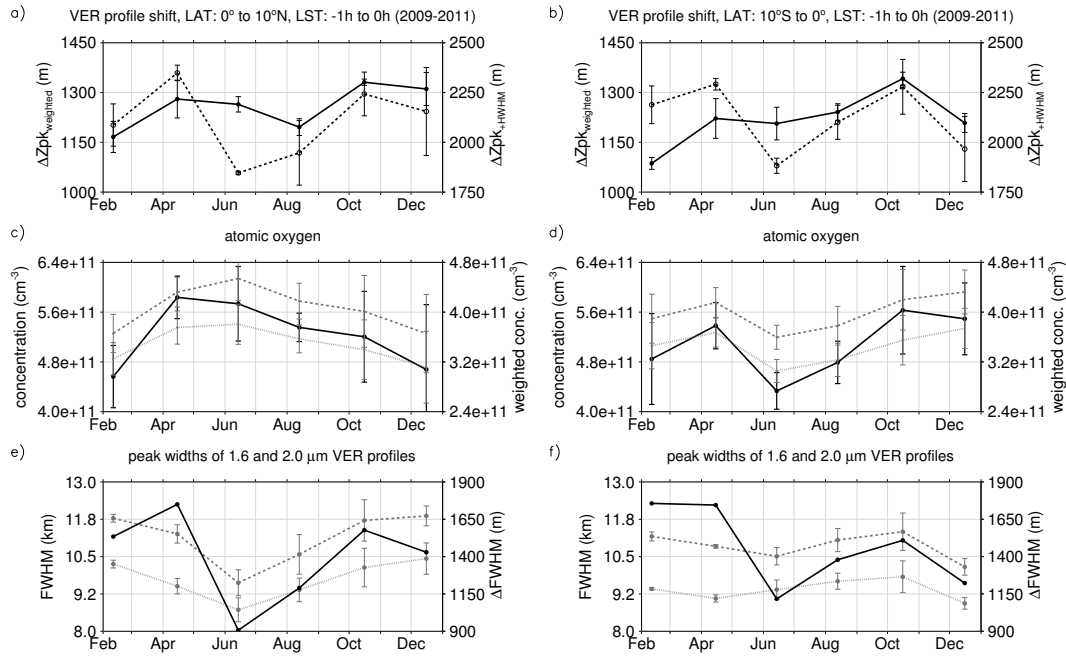


Fig. 5: SABER results based on three years of observation. Each point represents the mean value of three yaw cycles according to each year, the standard deviation is denoted by the error bars. Panel (a-b): Seasonal variability in the vertical shifts between the 1.6 and 2.0 μm VER profiles. Solid line/left axis: Vertical VER profile shifts between weighted peak altitudes according to Eq. (3). Dashed line/right axis: Vertical VER profile shifts between the +HWHM shifted peak positions according to Eq. (4). Panel (c-d): O concentrations at 90 km (left axis, black solid line) and 1.6 as well as 2.0 μm VER profile weighted atomic oxygen concentrations (right axis, dotted and dashed grey lines). Panel (e-f): Full peak widths of 1.6 and 2.0 μm VER profiles (dotted and dashed grey lines). Panel (e-f)/right axis: Relative difference between the full peak widths of the 1.6 and 2.0 μm VER profiles (black solid line).

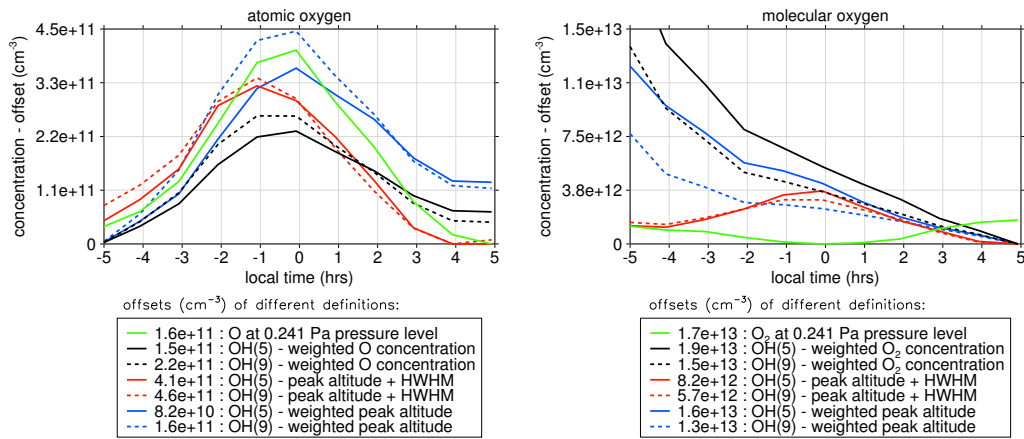


Fig. 6: Diurnal variability of simulated atomic and molecular oxygen concentrations. The same denotations apply that are used for the seasonal variability of both species in Fig. 3. The temporal averaging interval ranges from 15 September 2010 to 15 November 2010 to match the same period in our simulations that is needed for one complete SABER yaw cycle.

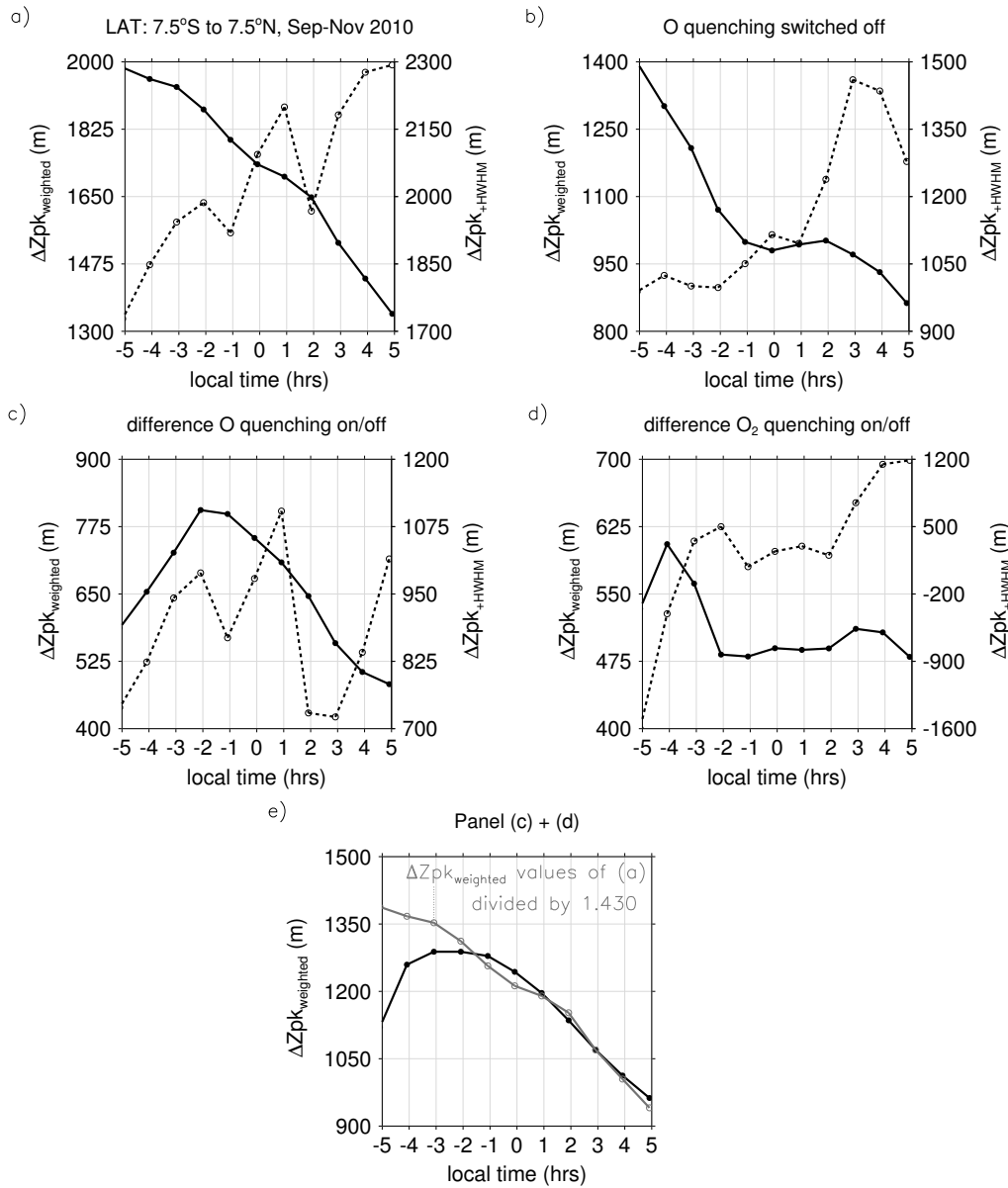


Fig. 7: Simulated diurnal evolution of vertical shifts at equatorial latitudes for the same averaging time as in Fig. 6. Panel (a): vertical shifts based on a model run including all quenching terms. The solid line refers to peak shifts with respect to weighted peak altitudes (Eq. 3), the dashed line refers to vertical shifts with respect to peak altitudes + HWHM (Eq. 4). Panel (b): peak shifts based on a model run with deactivated O quenching. Panel (c): Difference between Panel (a) and (b). Panel (c): Difference between a full quenching model run and a model run with deactivated O₂ quenching. Panel (e): Panel (c) + (d) (black line). Panel (f): Full peak width of the vibrationally integrated OH(ν) layer. Panel (f)/left axis: Full peak widths of OH(9) and OH(5) layers (dashed and solid grey lines). Panel (g)/right axis: Relative difference between the full peak widths of the OH(9) and OH(5) layers (black solid line).

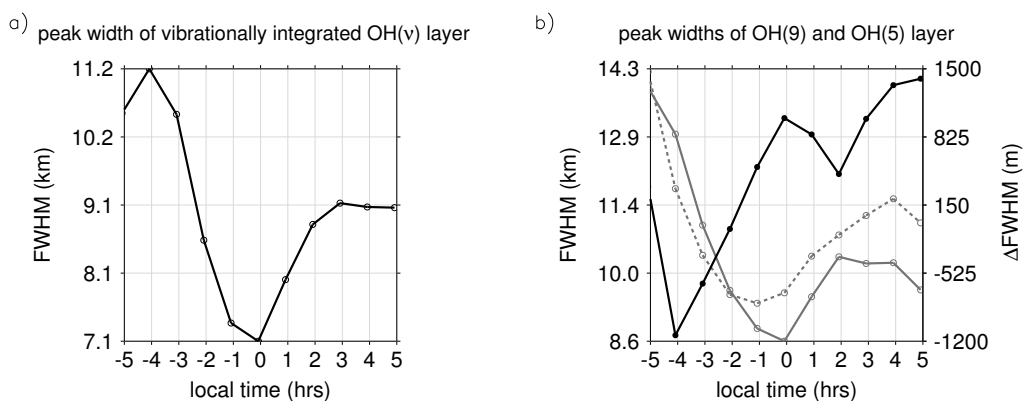


Fig. 8: Diurnal variability of OH peak widths for the same spatial and temporal bin considered in Fig. 7. Panel (a)/left axis: Full peak widths of OH(9) and OH(5) layers (dashed and solid grey lines). Panel (b)/right axis: Relative difference between the full peak widths of the OH(9) and OH(5) layers (black solid line).

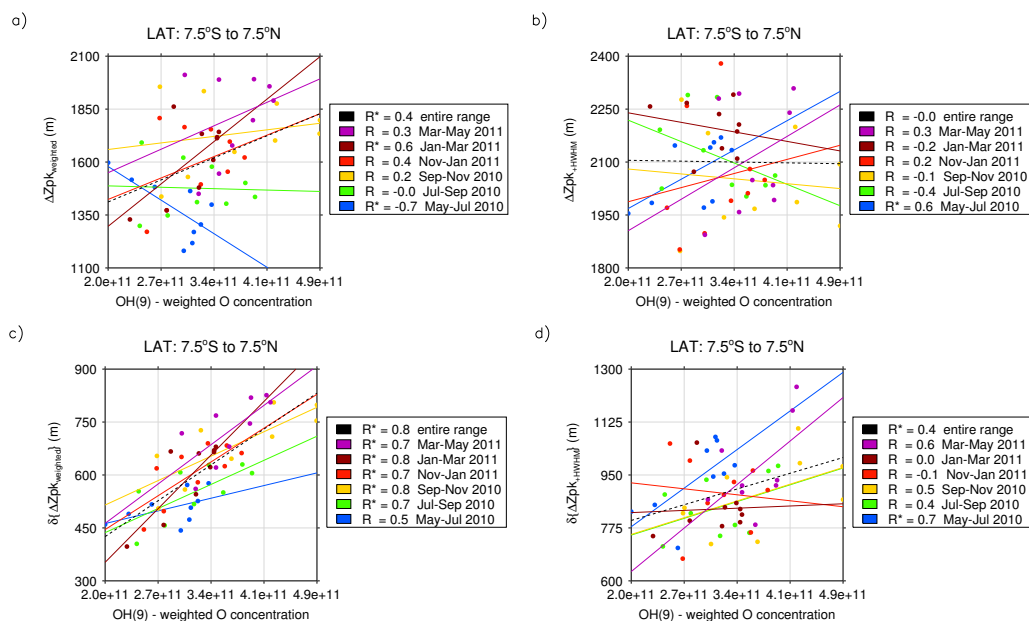


Fig. 9: Correlation plots of vertical OH(9;5) profile shifts (left panels Eq.3, right panels Eq.4) vs. OH(9) profile weighted O concentrations. The upper panels show the correlation between OH(9;5) profile shifts and O concentrations for the full quenching model run (similar to Fig. 7a). Similar to Fig. 7c, the lower panels consider the difference in vertical OH(9;5) profile shifts between the full-quenching and the deactivated O quenching model runs. Correlation coefficients are shown in the legend and denoted with the asterisk symbol *, if they were found to be significant according to a 90% significance level.

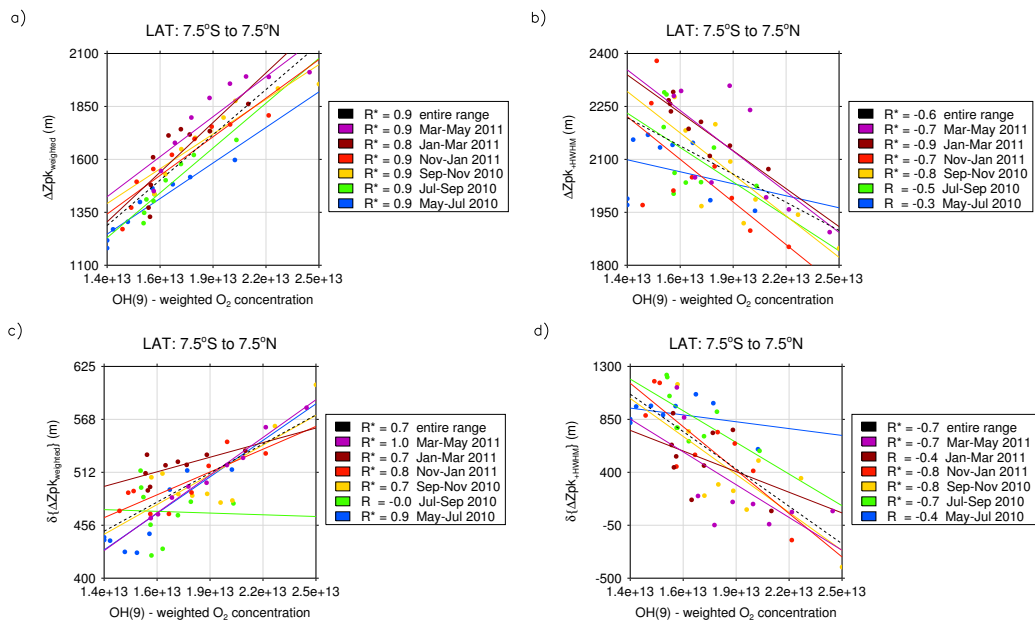


Fig. 10: Similar to Fig. 9 but referring to the O₂ quenching species.

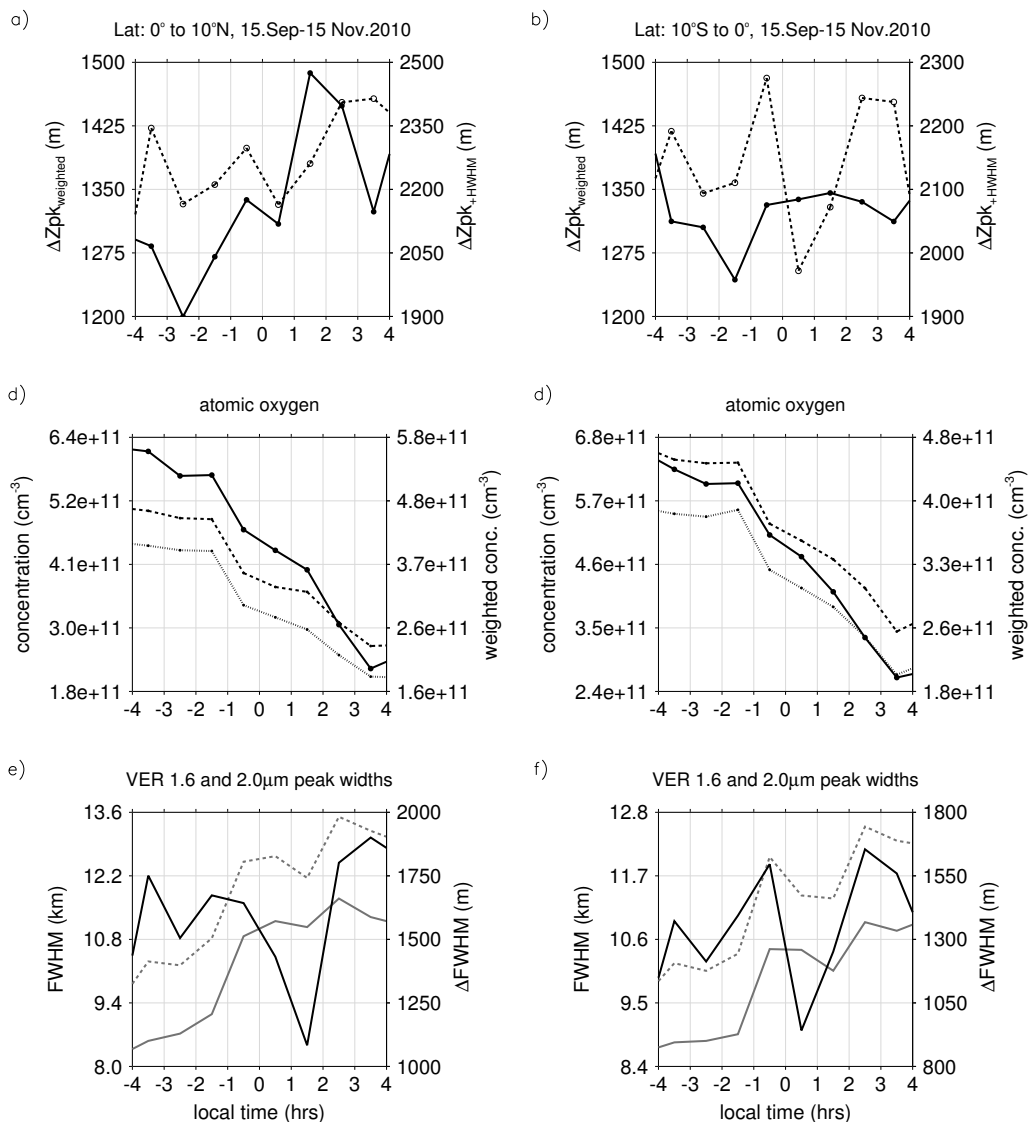


Fig. 11: Diurnal variability according to SABER OH observations. Panel (a-b): relative vertical OH peak shifts between VER(1.6 μm) and VER(2.0 μm) profiles in analogy with Fig. 7. Panel (c-d): O concentrations at 90 km level (left axis, solid line) and weighted with VER(1.6 μm) and VER(2.0 μm) (right axis, dotted and dashed line). Panel (e-f): FWHM of VER(1.6 μm) profile (grey dashed line), FWHM of VER(2.0 μm) profile (grey solid line) and the difference $\Delta FWHM$ between both FWHM values (black solid line).

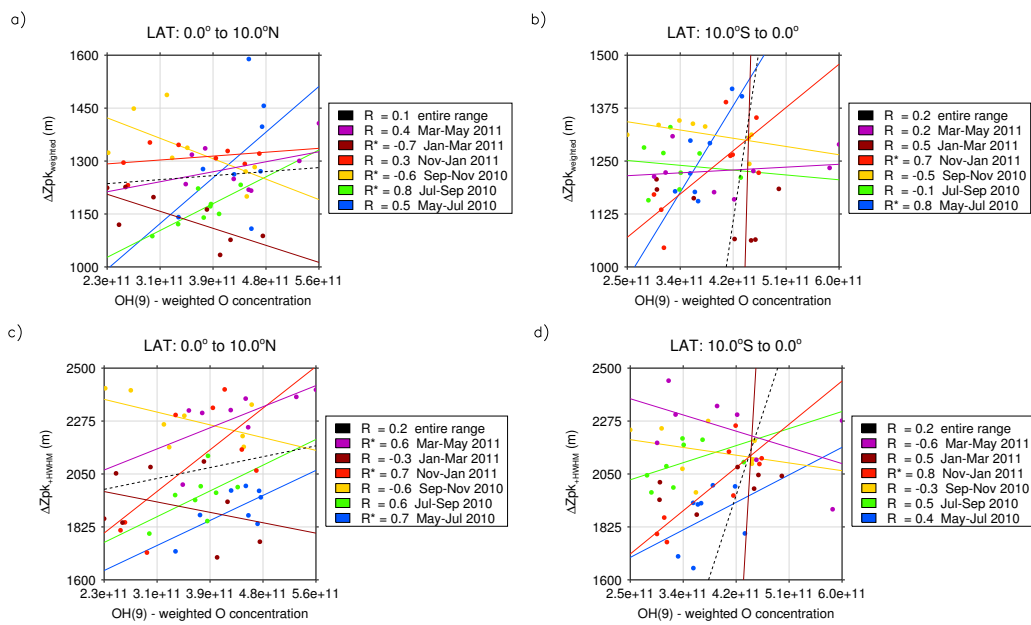


Fig. 12: Correlation between relative nighttime VER shifts and O concentrations from SABER observations in analogy with Fig. 9.